# Accuracy of internal fields in volume integral equation simulations of light scattering

Alfons Hoekstra, Jussi Rahola, and Peter Sloot

We studied the accuracy of volume integral equation simulations of internal fields in small particles illuminated by a monochromatic plane wave as well as the accuracy of the scattered fields. We obtained this accuracy by considering scattering by spheres and comparing the simulated internal and scattered fields with those obtained by Mie theory. The accuracy was measured in several error norms (e.g., mean and root mean square). Furthermore, the distribution of the errors within the particle was obtained. The accuracy was measured as a function of the size parameter and the refractive index of the sphere and as a function of the cube size used in the simulations. The size parameter of the sphere was as large as 10, and three refractive indices were considered. The errors in the internal field are located mostly on the surface of the sphere, and even for fine discretizations they remain relatively large. The errors depend strongly on the refractive index of the particle. If the discretization is kept constant, the errors depend only weakly on the size parameter. We also examined the case of sharp internal field resonances in the sphere. We show that the simulation is able to reproduce the resonances in the internal field, although at a slightly larger refractive index. 

*OCIS codes:* 290.0290, 290.5850.

## 1. Introduction

The role of large-scale simulations in research on light scattering by arbitrarily-shaped particles in the resonance regime (i.e., with dimensions comparable with the wavelength of the incident light) has gained increasing importance over the past decade; see e.g., Refs. 1–3. The best known, most widely used, and successful methods include the T-matrix approach,[4,5] the generalized multipole technique,[6] the multiple-multipole method,[7] and volume integral–based methods, such as the discrete dipole approximation[8] (DDA) and the volume integral equation formalism (VIEF; see Subsection 2.A below).[9–11]

As in all simulations we must have a good understanding of the errors that are introduced by the underlying model and by the numerical procedures. Ideally, a theoretical error analysis is combined with computations of errors, and model calculations are compared with real field experiments. All this is needed if we are to be able fully to control errors in a simulation. Unfortunately, in many cases we must do with much less. In our view the minimum set of error analysis should include computations of errors by comparison of simulation results with a set of known data stemming from, e.g., analytical results in special cases. Furthermore, we should have a procedure to determine the sensitivity of the simulation results in model parameters or numerical parameters. For instance, if simulations are performed on a grid, we should be able to check the convergence of the results by decreasing the grid dimensions and comparing the new results with previous results for coarser grids.

Simulations of elastic light scattering should of course obey the rules described above. Some authors were able to do a more-or-less complete analysis. For example, Hage and Greenberg, who simulated scattering by small porous cubes by using the VIEF method, compared their method against analytical results (Mie scattering) and against field experiments (microwave scattering by porous cubes), and they analyzed the sensitivity of the method for a number of parameters, such as the grid spacing.[12,13] However, usually the ideal set of error analysis results is not available. In many cases, simulation

A. Hoekstra and P. Sloot are with the Parallel Scientific Computing and Simulation Group, Faculty of Mathematics, Computer Science, Physics, and Astronomy, University of Amsterdam, Kruislaan 403, 1098 SJ Amsterdam, The Netherlands. The email address for A. Hoekstra is alfons@wins.uva.nl; the email address for P. Sloot is peterslo@wins.uva.nl. J. Rahola is with the Center for Scientific Computing, P.O. Box 405, FIN-02101 Espoo, Finland. The email address for J. Rahola is jussi.rahola@csc.fi.

Received 26 May 1998; revised manuscript received 28 September 1998.

0003-6935/98/368482-16$15.00/0

results for spheres are compared with Mie calculations in a limited range of size and refractive index.

In volume integral methods for scattering simulations, which are covered more extensively in Section 2, a formal solution of Maxwell's equations in the frequency domain is obtained numerically by the method of moments. The solution is the internal electric field in the particle, which we subsequently use to calculate cross sections and the scattering matrix of the particle. Error analysis in this case has almost always concentrated on the observable quantities, i.e., the scattered fields and cross sections (for a small overview, see Subsection 2.B). However, the basic physical quantity that is calculated is the internal field.

The errors in the scattered fields are a result of the errors in the internal field. Therefore, to understand better the behavior of errors in the volume integral method and if necessary to improve the method, an error analysis on the internal fields is also necessary. Furthermore, in some cases the internal field is the wanted quantity (see, e.g., Refs. 14–18), and in that case one must have an error analysis of the internal field simulations. Finally, a relationship between internal field resonances and the spectrum of eigenvalues of the interaction matrix exists. The spectrum in its turn determines the convergence of the iterative methods and the numerical errors in solving the method of moments equations.[19] A detailed and systematic study of internal field calculations in volume integral methods, and the associated errors, is therefore desirable.

In this paper we present computations by the VIEF method of internal fields for spheres illuminated by plane waves and compare the results with Mie calculations. As the range of our calculations is more extensive than in any publications of which we are aware, we report, in addition to the errors in the internal field, also those in the scattered fields.

We study the convergence of the VIEF method by keeping the size parameter and the refractive index of the sphere fixed, decreasing the grid spacing in the VIEF method, and monitoring the errors in the internal and scattered fields. Next, for three refractive indices, errors are obtained as a function of the size parameter of the sphere, up to a size parameter of 10. Finally, we study the special case of an internal field resonance in the sphere. Here we keep the size parameter of the sphere fixed and tune the sphere to a resonance by choosing an appropriate refractive index.

Throughout the paper we compute VIEF calculations of scattering by a sphere and compare them with the analytical Mie solution. The size of the sphere is given by the size parameter $x = 2\pi r/\lambda$, where $r$ is the radius of the sphere and $\lambda$ is the wavelength *in vacuo*.

## 2. Theory

### A. Volume Integral Equation Formalism

In this section we introduce the VIEF of electromagnetic scattering. First, the volume integral equation and its discretization are described. Next, we show how the resultant linear equations can be solved efficiently. We have chosen to work with the volume integral equation instead of the surface integral equation because the former permits a simple description of the scatterer in terms of cubic computational cells. Furthermore, it offers the possibility of computing scattering by inhomogeneous and anisotropic scatterers, and efficient numerical methods for solving the linear system in the volume integral equation formalism exist.

The volume integral equation of electromagnetic scattering is expressed as (for a derivation see, e.g., Refs. 9–11)

$$\mathbf{E}(\mathbf{r}) = \mathbf{E}_{\text{inc}}(\mathbf{r}) + k^3 \int_V [m(\mathbf{r}')^2 - 1]\mathbf{G}(\mathbf{r}, \mathbf{r}') \cdot \mathbf{E}(\mathbf{r}')\mathrm{d}^3 r', \tag{1}$$

where $\mathbf{E}(\mathbf{r})$ is the electric field inside the particle, $\mathbf{E}_{\text{inc}}(\mathbf{r})$ is the incident field, $k$ is the wave number, $m$ is the complex refractive index, $\mathbf{G}$ is the dyadic Green's function:

$$\mathbf{G}(\mathbf{r}, \mathbf{r}') = \left(\mathbf{1} + \frac{\nabla\nabla}{k^2}\right) g(|\mathbf{r} - \mathbf{r}'|),$$

and

$$g(r) = \frac{\exp(ikr)}{4\pi kr}.$$

In the three equations above, we assume that the electric field has the harmonic time dependence $\exp(-i\omega t)$.

The integral equation can be discretized in various ways. The simplest discretization uses cubic cells and assumes that the electric field is constant inside each cube (the piecewise-constant approximation). By requiring that integral equation (1) be satisfied at the centers $\mathbf{r}_i$ of the $N$ cubes (the point-matching or collocation technique) and by using simple one-point integration, we end up with the equation[9,10]

$$\left\{1 - [m(\mathbf{r}_i)^2 - 1]\left(k^3 M - \frac{1}{3}\right)\right\}\mathbf{E}(\mathbf{r}_i) = \mathbf{E}_{\text{inc}}(\mathbf{r}_i) + \frac{k^3 V_1}{4\pi} \sum_{\substack{j=1 \\ j \neq i}}^{N} [m(\mathbf{r}_j)^2 - 1]\mathbf{T}_{ij} \cdot \mathbf{E}(r_j),$$

where $i = 1, \ldots, N$, $V_1$ is the volume of the computational box, $M$ is given by

$$M = \frac{2}{3k^3}\{[1 - ikd(3/4\pi)^{1/3}]\exp[ikd(3/4\pi)^{1/3}] - 1\},$$

$d$ is the length of side of the computational box, and $\mathbf{T}_{ij}$ is given by

$$\mathbf{T}_{ij} = \frac{\exp(i\rho_{ij})}{\rho_{ij}^3}(\rho_{ij}^2 + i\rho_{ij} - 1)\mathbf{1} + \frac{\exp(i\rho_{ij})}{\rho_{ij}^3}(-\rho_{ij}^2 - 3i\rho_{ij} + 3)\hat{\mathbf{r}}_{ij}\hat{\mathbf{r}}_{ij},$$

$$\rho_{ij} = k|\mathbf{r}_i - \mathbf{r}_j|,$$

$$\hat{\mathbf{r}}_{ij} = (\mathbf{r}_i - \mathbf{r}_j)/|\mathbf{r}_i - \mathbf{r}_j|.$$

The factor $M$ arises from the analytical integration of the self term from use of a sphere whose volume is equal to the volume of the cube.[9,10] The matrix $\mathbf{T}_{ij}$ can be interpreted as a dipole radiation term; i.e., the cubes couple with one another through a dipole radiation field.

To improve the accuracy of the VIEF, more-refined discretization schemes could be used. The electric field inside each computational cube could be expanded in higher-order polynomial basis functions or vector spherical waves, as was done by Peltoniemi.[20] Instead of from the collocation method, the system of linear equations could be obtained from the Galerkin or the least-squares method.

When the point-matching technique described above and the piecewise-constant basis functions are used, the VIEF is mathematically and computationally similar to the DDA.[8,21,22] Lakhtakia has shown that the DDA and the VIEF are mathematically equivalent, except for the self term.[23,24] In the DDA many formulations for the self term exist (see, e.g., Ref. 8), and some of them are quite similar to the VIEF. In practice, on many occasions DDA and VIEF simulations result in almost comparable numerical values. One of the advantages of the VIEF over the DDA is that for the former no effective-medium theories are needed and thus no free parameters are introduced.

The VIEF requires the solution of a large system of linear equations in which the coefficient matrix is complex symmetric. The efficient solution of these equations by various iterative solvers has been studied by Rahola.[25] The quasi-minimal residual method of Freund[26] turned out to be best suited to this problem.

The computationally most intensive operation in the iterative solution of dense linear systems is the computation of the matrix–vector product. For our scattering calculations we can compute the matrix–vector product without actually forming the coefficient. When a volumetric scatterer is enlarged to a cube by addition of ghost cubes, the matrix–vector product reduces to a three-dimensional (3D) convolution that can be computed efficiently with a 3D fast Fourier transform.[27] This is the method that we used in our test calculations. The fast Fourier transform was also used in the DDA calculations by Hoekstra *et al.* to compute scattering by use of models with as many as seven million dipoles.[28,29]

### B. Some Previous Results of Error Analysis

The VIEF and the DDA are similar, and therefore we introduce previous studies of the accuracy of both methods. As far as we know, no previous research has addressed the accuracy of internal fields obtained with VIEF simulations of scattering. In all cases the accuracy of scattered fields was measured by comparing them with analytical results, with real experiments, or with other calculations.

Draine has shown a limited set of results for polarization of the dipoles in DDA simulations of spheres in the long-wavelength limit.[30] He shows that the errors in the polarization (direction and magnitude) increase with increasing refractive index, decrease with smaller dipole sizes (i.e., with a finer discretization), and appear to be largest near the surface of the sphere. These errors are attributed to the surface granularity of the model and to less-effective screening of the dipoles from the incident field.

Hage and Greenberg compared VIEF results for scattered intensity and linear polarization for $x = 1$, 3, 5 and $m = 1.33$ with Mie calculations.[12,13] In all cases they applied a model containing 1064 cubes. They therefore needed to increase the size of the cubes to increase the size parameter of the sphere. This requirement makes it, in our view, difficult to interpret the results, which show a decreasing accuracy in the VIEF for increasing size parameter. Hage and Greenberg also compared $C_{ext}$ results from the VIEF with those of DDA calculations, using Draine's DDA formulation of 1988.[30] Hage and Greenberg showed that the DDA and the VIEF result in a comparable accuracy; however, for larger cube sizes the VIEF performs better.

Recently Draine and Goodman showed that a new formulation of the DDA, which uses the lattice dispersion relation to calculate the polarizability of the dipoles, performs better than the original DDA and also gives better results than the VIEF.[31] They reported performing an extended set of tests of the accuracy of the DDA by use of the lattice dispersion relation to calculate cross sections. In all cases a sphere was modeled with 17,904 dipoles (cubes), and again the size parameter of the sphere was changed by changing the size of the dipoles. The main conclusion is that for small values of $m$ the DDA and the lattice dispersion relation (and also the VIEF) yield accurate results ($\leq$2%) for $|m|d/\lambda < 0.1$, where $d$ is the size of a single dipole in the DDA or is the cube size in the VIEF. Larger values of $m$ result in somewhat smaller accuracy, and for extremely large absorption the errors become much larger. Especially for $C_{abs}$, the errors can be as large as 20%. The exact source of these errors remains unclear. These results, however, were restricted to total cross sections.

In Ref. 8 Draine and Flatau presented more results on the accuracy of the DDA and also for errors in differential scattering. Root-mean-square (rms) errors in the differential scattering were shown to be of the order of a few percent, provided that $|m|d/\lambda < 0.1$. However, for specific scattering angles the er-

ors could be as large as 15%. All the results of Draine and co-workers were in the range $1 \le x \le 7$ and $m = 1.33 + 0.01i$, $m = 1.7 + 0.1i$, $m = 2 + i$, and $m = 3 + 4i$. They did not show results for other scattering matrix elements than $S_{11}$, except for the case of a simulation of two spheres in contact, where $S_{22}$ results were reported.

An important parameter in the accuracy of the VIEF and the DDA is the size of the cubic cells (or dipoles). Many authors have tested this dependence (see, e.g., Ref. 8 and references therein and Refs. 31 and 32), and they all conclude that accurate results can be obtained if $\mathrm{Re}(m)d/\lambda < 0.1$. Furthermore, the effect of surface granularity on the accuracy of simulations of the $S_{34}$ scattering matrix element was discussed in Ref. 32. Therefore here we take the size of the cubic cells in the VIEF simulations as a separate parameter and investigate its influence on the internal fields while keeping other parameters fixed.

### C. Resonances in Mie Scattering

When we are computing the internal and scattered electric fields for a sphere, the fields typically change smoothly when the size of the sphere or the index of refraction is varied. However, some combinations of values of the size parameter and the index of refraction give rise to a sharp resonance in the Mie solution, where a single mode of the vector spherical harmonics is greatly amplified. The resonance clearly shows up in the internal field and cross sections. We want to test whether the VIEF is able to reproduce such resonances.

In this section we first give some background information on the resonances. In Subsection 4.D we show how the VIEF calculations behave in the neighborhood of a resonance. The resonance is a fairly difficult test for the VIEF, as the resonance peaks can be quite narrow and thus difficult to locate exactly and because the coefficient matrix becomes singular at a resonance.

In the Lorenz–Mie solution the incident, internal, and scattered fields are expanded in terms of the vector spherical harmonics; see, e.g., Bohren and Huffman.[33] Consider scattering by a sphere with size parameter $x$ and refractive index $m$. The Mie coefficients of the scattered field are

$$a_n = \frac{m\psi_n(mx)\psi_n'(x) - \psi_n(x)\psi_n'(mx)}{m\psi_n(mx)\xi_n'(x) - \xi_n(x)\psi_n'(mx)},$$

$$b_n = \frac{\psi_n(mx)\psi_n'(x) - m\psi_n(x)\psi_n'(mx)}{\psi_n(mx)\xi_n'(x) - m\xi_n(x)\psi_n'(mx)},$$

and the coefficients for the internal field are

$$c_n = \frac{m\psi_n(x)\xi_n'(x) - m\xi_n(x)\psi_n'(x)}{\psi_n(mx)\xi_n'(x) - m\xi_n(x)\psi_n'(mx)},$$

$$d_n = \frac{m\psi_n(x)\xi_n'(x) - m\xi_n(x)\psi_n'(mx)}{m\psi_n(mx)\xi_n'(x) - \xi_n(x)\psi_n'(mx)}.$$

Here the Riccati–Bessel functions are

$$\psi_n(x) = xj_n(x), \qquad \xi_n(x) = xh_n(x),$$

where $j_n(x)$ and $h_n(x)$ are the spherical Bessel and Hankel functions, respectively.

Resonances arise when the denominator in the coefficient $a_n$, $b_n$, $c_n$, or $d_n$ becomes small. Note that the denominators of $a_n$ and $d_n$ are identical, and so are those of $b_n$ and $c_n$. This means that an internal field mode ($c_n$ or $d_n$) and a scattered field mode ($b_n$ or $a_n$) are resonant for the same combination of $x$ and $m$.

It has been shown that the denominators can be exactly zero only if either $x$ or $m$ is complex. Furthermore, if $x$ is real then $m$ must have a negative imaginary part corresponding to negative absorption.[34,35] However, in some cases the resonance can occur if $x$ is real and the negative imaginary part of $m$ is small. In these situations the resonance also appears if we replace $m$ by its real part, and the sharpness and strength of the resonance are determined by the imaginary part of $m$. A similar reasoning applies if we keep $m$ real and look at complex values of $x$.

If $m$ and $x$ are real, we can write the coefficients $a_n$, $b_n$, $c_n$, and $d_n$ in the following form:

$$a_n(x, m) = \frac{A_n(x, m)}{A_n(x, m) - iC_n(x, m)},$$

$$b_n(x, m) = \frac{B_n(x, m)}{B_n(x, m) - iD_n(x, m)},$$

$$c_n(x, m) = \frac{im}{B_n(x, m) - iD_n(x, m)},$$

$$d_n(x, m) = \frac{im}{A_n(x, m) - iC_n(x, m)}.$$

The functions $A_n$, $B_n$, $C_n$, and $D_n$ are real. In the resonance positions either $C_n = 0$ or $D_n = 0$, forcing $a_n$ or $b_n$ to be 1. If, in that case, $A_n$ or $B_n$ is small, the internal field at a resonance can become large.

Resonances show up as sharp peaks in graphs of the extinction coefficient as a function of the size parameter. Usually authors use relatively large size parameters when they study the resonances (see, e.g., Ref. 36 and references therein). However, because of computer memory and CPU time limitations we were, in our simulations, forced to keep the size parameter limited. Therefore we decided to look for resonances that have a small, fixed size parameter. We now find the resonances by tuning the refractive index. Therefore, in contrast with other authors, we study the extinction coefficient as a function of the refractive index to identify the resonances.

We have chosen to analyze scattering near two resonances. The $a_7$, $d_7$ mode becomes resonant if $x = 4.875$ and $m = 2.3009279–0.002757527i$. Similarly, the $b_8$, $c_8$ mode becomes resonant for $x = 4.875$ and $m = 2.3534695–0.0005001699i$. As the $a$-type modes are TM fields and the $b$-type modes are TE fields,[33] the first resonance is identified as a seventh-

order TM resonance, and the second as an eighth-order TE resonance.

In the simulations we assume a real refractive index (i.e., set the small imaginary part to zero). As will be shown in Subsection 4.E, these values for $x$ and $m$ give rise to strong resonances.

## 3. Methods

We measure the accuracy of the internal fields obtained by VIEF by simulating scattering by spheres and comparing the results with Mie calculations. A sphere is discretized into $N$ cubes. The internal field is calculated by numerical solution of Eq. (1), as was described in Subsection 2.A. The internal field is obtained on the center point of each cube. This field is denoted $\mathbf{E}^i_{\text{VIEF}}$, where the superscript $i$ refers to the field in the center of cube $i$. The exact Mie solution is also calculated in the centers of the cubes and is denoted $\mathbf{E}^i_{\text{Mie}}$. The difference field is defined as

$$\mathbf{E}^i_{\text{diff}} = \mathbf{E}^i_{\text{Mie}} - \mathbf{E}^i_{\text{VIEF}}. \tag{2}$$

This difference field is the basis on which we obtain values for the accuracy of the internal field. In all simulations we assume that the sphere is centered at the origin and that the incident field is an $x$-polarized plane wave traveling in the positive $z$ direction.

The model parameters are the size parameter $x$ and the complex refractive index $m$ of the sphere and the size of cubes in the VIEF method, $d = \lambda/\text{cpwl}$, where cpwl means cubes per wavelength. In what follows, we assume that the wave number $k = 2\pi/\lambda$ is set to 1 (i.e., the size parameter $x$ is equal to the radius $r$ of the sphere). Furthermore, the size of the cubes is always specified in terms of the cpwl parameter. The accuracy of the internal and scattered fields is measured as a function of these three parameters.

In VIEF simulations the sphere is modeled with $N$ cubic cells. The cubic cells are positioned upon a grid as described, e.g., in Ref. 8, and the radius of the sphere is such that it has the same volume as the total volume occupied by all cubic cells in the model of the sphere.

The data sets are analyzed in a number of different ways. The first method is by visualization. The electric fields $\mathbf{E}^i_j$ (where $j$ means the subscript Mie, VIEF, or diff) are 3D complex vector fields and are therefore difficult to visualize. A first approach is to calculate the energy density:

$$s^i_j = (\mathbf{E}^i_j)^* \mathbf{E}^i_j, \tag{3}$$

where * denotes complex conjugation. This scalar field is a measure of the intensity of the electric field and can be plotted in color plots in a full 3D projection or in planes through the sphere. The last-named method was applied by many other authors (see, e.g., Refs. 37 and 38). In this paper we present a number of examples of such visualizations. Another way to visualize the data is to plot vector fields, which we obtain by taking either the real or the imaginary parts of $\mathbf{E}^i_j$.

In this paper a number of examples of internal field visualizations are shown as gray-scale plots. We have prepared an accompanying document, available on the World Wide Web, from which the color versions of the figures in this paper and a number of other examples of internal field visualizations can be obtained.[39]

A final technique that has proved useful is to plot the amplitude of the electric fields as a function of the distance to the center of the sphere. Although no azimuthal information remains, such plots give much information with respect to the distribution of, e.g., the errors in the internal field.

Although visualization is an indispensable tool in helping in our understanding of the data sets, we also need quantitative error norms. The great amount of data (here $N$ can be as large as $10^5$) forces the use of statistical error norms.

Define the absolute error in the internal field on a point in the sphere as

$$\varepsilon^i_{\text{abs}} = |\mathbf{E}^i_{\text{diff}}|$$

and the relative error as

$$\varepsilon^i_{\text{rel}} = |\mathbf{E}^i_{\text{diff}}|/|\mathbf{E}^i_{\text{Mie}}|.$$

Next, for both absolute and relative errors the minimum, the maximum, the mean, the standard deviation, and the rms errors over all cube positions are calculated, yielding a good amount of data reduction. As is shown in Section 4, in most cases the rms, combined with the maximum error, provides good insight into the distribution of the errors.

We briefly discuss the error analysis of the scattered fields. The nonzero elements of the scattering matrix, i.e., $S_{11}$, $S_{12}/S_{11}$, $S_{33}/S_{11}$, and $S_{34}/S_{11}$ are calculated as a function of the scattering angle, usually in steps of 1 deg. Note that $S_{12}$, $S_{33}$, and $S_{34}$ are all normalized with $S_{11}$. In this way these elements are always between 1 and $-1$. Next, for each scattering angle the relative error in $S_{11}$ is calculated, as is the absolute error for the other three (normalized) matrix elements. Again, from the resultant sets of errors the minimum, the maximum, the mean, the standard deviation, and the rms errors over the scattering angles are calculated. Finally, the extinction coefficient $C_{\text{ext}}$, the absorption coefficient $C_{\text{abs}}$, and the scattering coefficient $C_{\text{scat}}$ are calculated. From these values the absolute errors and the relative errors between the VIEF and Mie results are obtained.

## 4. Results

### A. Introduction

We performed three types of experiment. First we investigated the convergence of VIEF simulations in the limit of small discretization. Spheres with constant size parameters and with three different refractive indices were considered. As we varied the sizes of the cubes, we compared the VIEF results with the exact Mie results. Next we investigated the accuracy of VIEF simulations as a function of the size

Table 1. Overview of Size Parameter and Refractive Index of the Three Spheres Studied in This Section[a]

| Sphere Number | Size Parameter | Refractive Index | cpwl | cpwl/Re($m$) | $N$ |
|---|---|---|---|---|---|
| 1 | 9 | 1.05 | 15 | 14.3 | 41,472 |
| 2 | 9 | 1.33 + 0.01$i$ | 20 | 15.0 | 98,512 |
| 3 | 5 | 2.5 + 1.4$i$ | 35 | 14.0 | 90,536 |

[a]The cpwl parameter is the cubes-per-wavelength parameter used in the VIEF simulation, and $N$ is the number of cubes in the VIEF simulation.

parameter of the spheres, also for three different refractive indices. Finally, the behavior of VIEF simulations near a structural Mie resonance was investigated. In all cases the accuracy of the internal and scattered fields was obtained, as described in Section 3, and all data sets were analyzed by the methods of Section 3. Here we can present only a small part of all data sets.

In all experiments three refractive indices, $m$ = 1.05, $m$ = 1.33 + 0.01$i$, and $m$ = 2.5 + 1.4$i$, were used. In this way we covered the range of very small refractive index (for, e.g., biological particles), moderate refractive index (water, dirty ice), and very high refractive index with large absorption (for, e.g., graphite). All size parameters in the experiments were in the range 1–10. The largest VIEF models contained of the order of $10^5$ cubes.

In Subsection 4.B three case studies of VIEF simulations are presented in some detail. The goal is to provide insight into the wealth of information that is generated in the experiments and to prepare for what follows. In Subsection 4.C the results of the convergence studies are presented, and in Subsection 4.D those for the size dependence are given. Finally, in Subsection 4.E the results for the resonances are presented.

### B. Three Case Studies

Here we consider the internal and scattered fields of three different spheres (see Table 1). The number of cubes per wavelength for the VIEF simulations is chosen such that cpwl/Re($m$) is approximately the same for all three spheres.

In Fig. 1 we show the internal field for the spheres of Table 1 by plotting the energy density in a plane through the sphere in a surface plot. Only the Mie results are drawn. The energy density of the difference field is shown in Fig. 2. Note that we do not plot the energy density exactly through a symmetry plane (i.e., the $y$ = 0 plane) because in the VIEF simulation the cubes are arranged symmetrically about the $x, y, z$ = 0 planes, and the VIEF calculates the electric fields at the centers of the cubes. In fact, we plot the energy density on the plane closest to the $y$ = 0 plane.

One can observe three typical internal field distributions (see Fig. 1). For a small refractive index the internal field is almost equal to the incident field. The energy density of the incident field, which is a plane wave, is equal to 1 everywhere. As can be

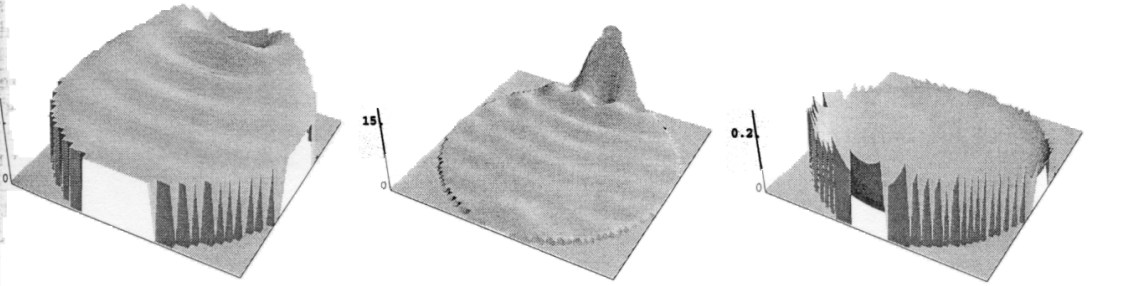


Fig. 1. Energy density for the internal field obtained by Mie calculation. Left, sphere 1 ($x$ = 9, $m$ = 1.05, plotted in the $y$ = 0.21 plane); middle, sphere 2 ($x$ = 9, $m$ = 1.33 + 0.01$i$, plotted in the $y$ = 0.157 plane); right, sphere 3 ($x$ = 5, $m$ = 2.5 + 1.4$i$, plotted in the $y$ = 0.09 plane). All scales in the plots are linear.

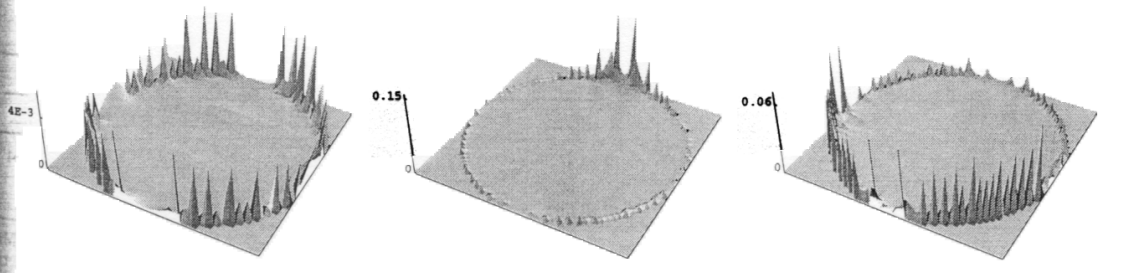


Fig. 2. Same as in Fig. 1 but for the energy density for the difference field defined in Eq. (2).

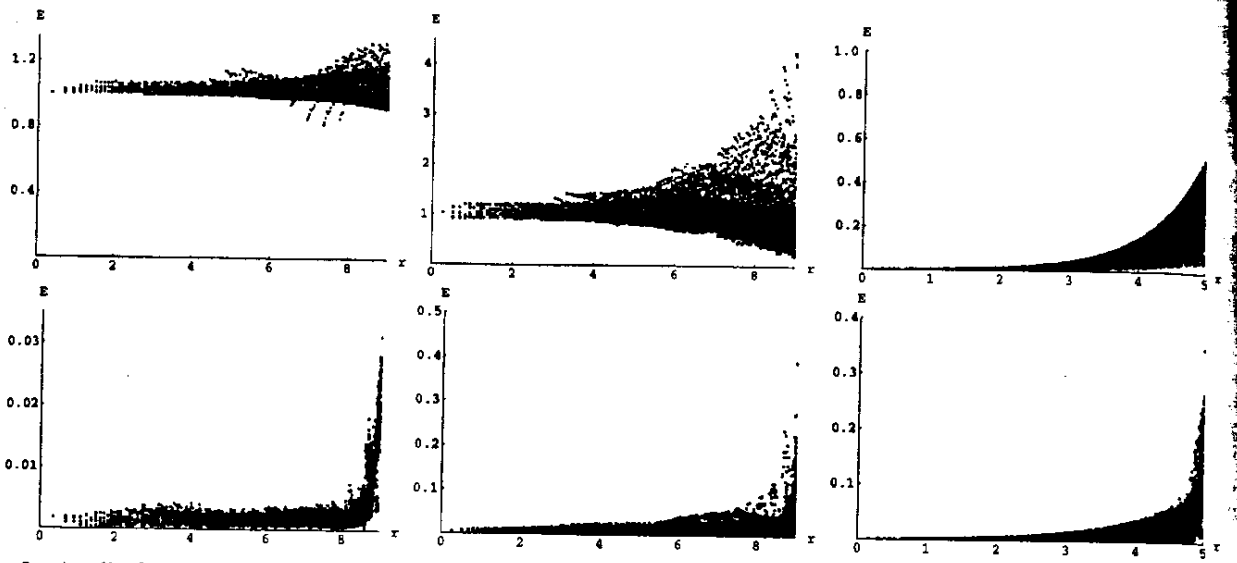

Fig. 3. Amplitudes of top, the internal Mie field and bottom, difference field as functions of radial distance in the sphere. Left, sphere 1; middle, sphere 2; right, sphere 3. (See Table 1 for properties of the spheres.)

seen from Fig. 1, for sphere 1 the energy density is everywhere very close to 1. Also, by looking at the color density plots and the vector plots (see the WWW site 39) we can see that the internal field in this case is a slightly distorted plane wave. For the larger refractive index of sphere 2 we see a clear difference between the internal field and the incident field, and we observe a typical interference peak at the far end of the particle. Finally, for sphere 3, with large absorption, we can see that the internal field is very small, except at the surface. Furthermore, the fields are strongest at the front end of the particle. These types of internal field are in agreement with the cases surveyed by Dobson and Lewis.[37] As can be inferred from Figs. 1 and 2, in all three cases the errors in the VIEF internal fields are largest on the surface of the sphere.

Another way to look at the internal field is to plot its amplitude, and the amplitude of the difference field, as a function of the radial distance in the sphere, as demonstrated in Fig. 3. Again, the three different types of internal field distribution are clearly seen. Also, the distribution of the errors in internal VIEF field is now clearly visible. Looking at the absolute numbers in Fig. 3 already suggests that the absolute and the relative errors increase with increasing refractive index of the spheres.

Table 2 lists the statistical averages of the absolute and the relative errors in the internal fields (as defined in Section 3) for the three spheres. In all our experiments the mean error and the standard deviation are comparable and the rms is usually somewhat larger. The minimum error is usually much smaller than the mean error. The maximum error usually is much larger than the rms. Listing the rms and the maximum error provides sufficient statistical information with which to interpret the data sets.

Finally we turn our attention to the scattered fields. Table 3 lists the cross sections obtained by VIEF simulations and by Mie scattering and the relative errors. Figures 4–6 show the scattering matrix elements as a function of the scattering angle for both VIEF and Mie calculations. The agreement between Mie and VIEF calculations is generally good. Only for the large-refractive-index case (sphere 3; see Fig. 6) does the VIEF seem to produce somewhat larger errors, especially for the $S_{12}$, $S_{33}$, and $S_{34}$ elements of the scattering matrix. Note, however, that $S_{11}$ is drawn on a logarithmic scale, which makes

Table 2. Errors in the VIEF Simulations of the Internal Fields for the Spheres Defined in Table 1[a]

| Sphere Number | Absolute Error | | | | | Relative Error (%) | | | | |
|---|---|---|---|---|---|---|---|---|---|---|
| | Min | Mean | SD | RMS | Max | Min | Mean | SD | RMS | Max |
| 1 | $9 \times 10^{-5}$ | $3 \times 10^{-3}$ | $4 \times 10^{-3}$ | $5 \times 10^{-3}$ | 0.03 | 0.09 | 0.3 | 0.4 | 0.5 | 3.4 |
| 2 | $1 \times 10^{-3}$ | 0.02 | 0.02 | 0.03 | 0.5 | 0.1 | 1.9 | 2.0 | 2.8 | 19 |
| 3 | $2 \times 10^{-4}$ | 0.02 | 0.03 | 0.04 | 0.35 | 0.9 | 21 | 12 | 23 | 120 |

[a]Error norms are shown for absolute and relative errors, as defined in Section 3; Min is the minimum error in the internal field, Max is the maximum error; Mean is the mean error averaged over all cubes and SD is the associated standard deviation; rms is the root-mean-square error calculated over all cubes.

Table 3. Scattering Cross Sections for Spheres 1–3 for Mie Calculations and VIEF Simulations and Relative Errors[a]

| Sphere Number | $C_{ext}$ | | | $C_{scu}$ | | | $C_{abs}$ | | |
|---|---|---|---|---|---|---|---|---|---|
| | Mie | VIEF | Error (%) | Mie | VIEF | Error (%) | Mie | VIEF | Error (%) |
| 1 | 100.19 | 100.14 | 0.05 | 100.19 | 100.14 | 0.05 | 0 | 0 | 0 |
| 2 | 697.5 | 698.0 | 0.07 | 607.9 | 608.8 | 0.1 | 89.6 | 89.2 | 0.5 |
| 3 | 207.3 | 210.4 | 1.5 | 118.4 | 118.0 | 0.3 | 88.8 | 92.4 | 4.0 |

[a]Properties of spheres are defined in Table 1.

it difficult to assess the errors by visual inspection of the figures.

In Table 4 the statistical errors over the scattering angles (only rms and maximum) are shown for the scattering matrix elements. The table shows that for the three spheres the results are comparable, except for the $S_{34}$ element. For this element sphere 3 clearly has larger errors. The numbers in Table 3,

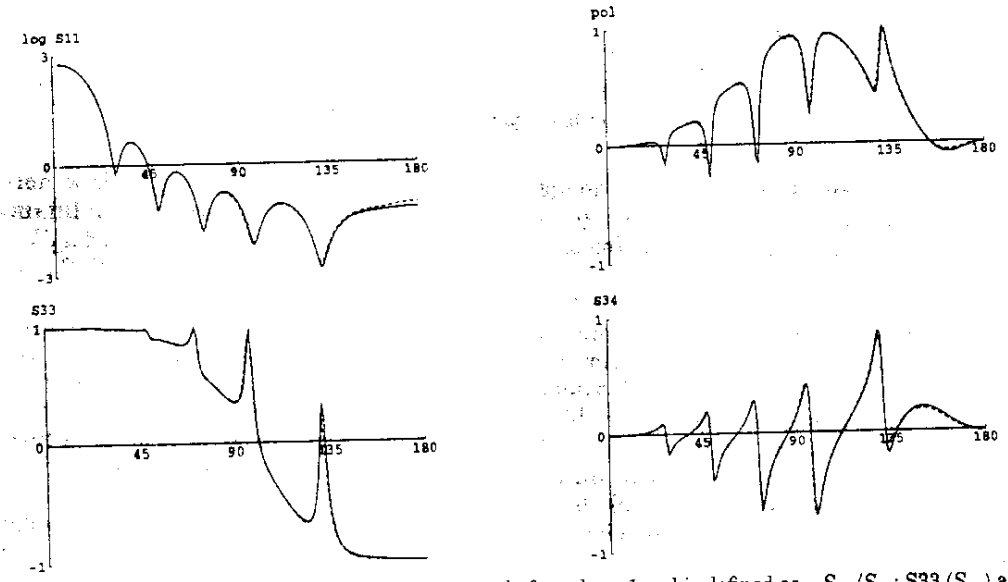


Fig. 4. Scattering matrix elements as a function of scattering angle for sphere 1; pol is defined as $-S_{12}/S_{11}$; S33 ($S_{33}$) and S34 ($S_{34}$) are normalized by S11 ($S_{11}$). Solid curves, Mie results; dashed curves, VIEF results.

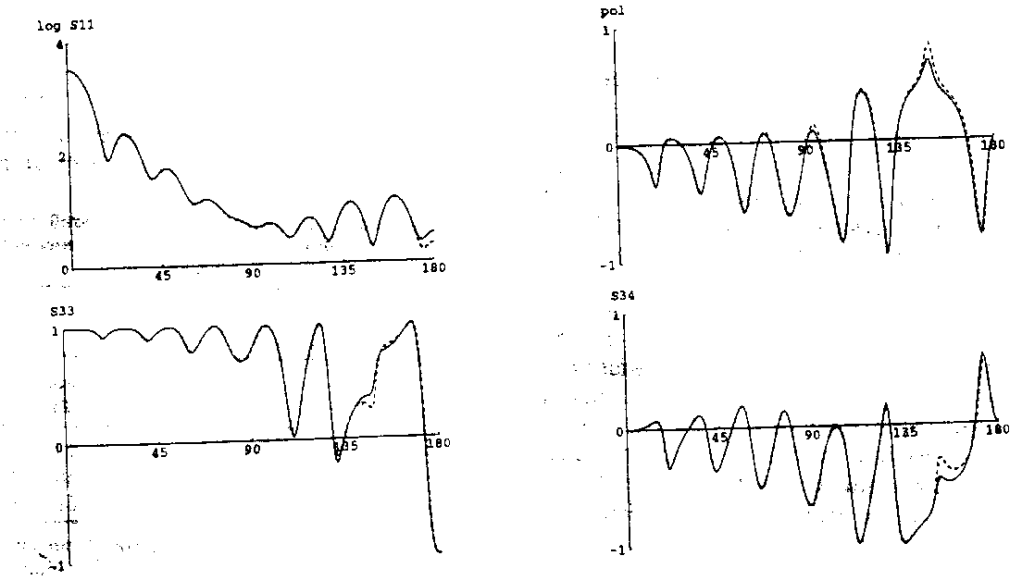


Fig. 5. Same as Fig. 4 but for sphere 2.

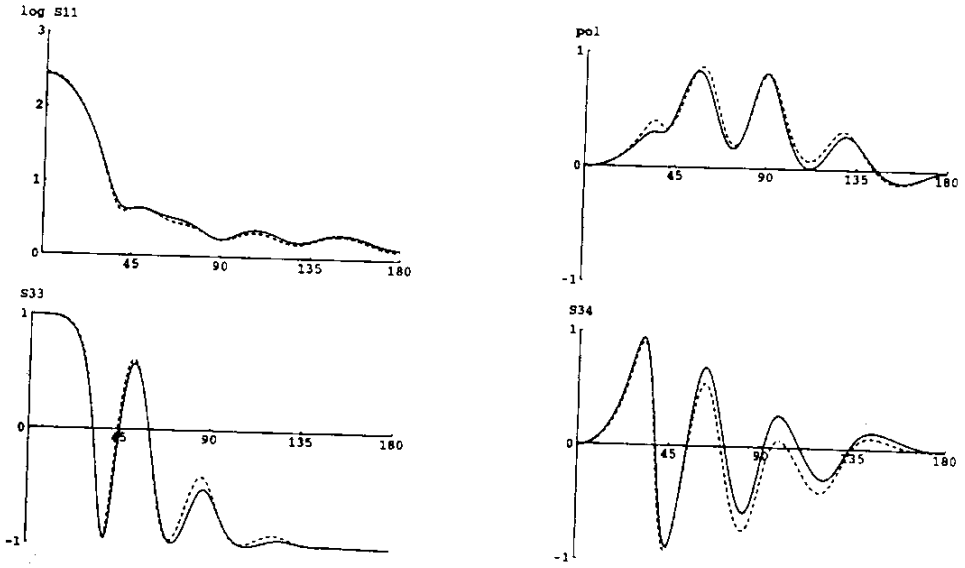


Fig. 6. Same as Fig. 4 but for sphere 3.

in combination with Figs. 4–6, show also that we have to be careful in interpreting the numbers. For example, the $S_{12}/S_{11}$ elements of the scattering matrix for spheres 2 (Fig. 5) and 3 (Fig. 6) have comparable statistical error norms, although the figures suggest that the result for sphere 2 is better than for sphere 3. We should realize that in case of a sharp minimum or maximum, as for the polarization of sphere 2, a slight error in the position of the extremum can result in relative large differences between the Mie and VIEF functions and thus in relative large rms values.

In what follows we report rms values for the errors in the scattering matrix. We must, however, keep in mind, as in the example above, that two equal rms values can be due to different phenomena (i.e., a slight overall error versus large errors located near certain scattering angles). Therefore in a detailed interpretation of the statistical error norms it is always necessary to go back to the original data.

### C. Convergence

Here we test the convergence of VIEF simulations with respect to grid refinement. For a number of spheres the number of cubes per wavelength is gradually increased and the results are compared with Mie calculations. The convergence is tested for the same three refractive indices that were used in Subsection 4.B (see Table 1) and for three different size parameters ($x = 3, 5, 9$). The internal fields in these convergence tests are all comparable with those shown in Fig. 1 and 3. The errors in the internal fields also behave similarly to those in Figs. 2 and 3. Therefore here we present only the errors of the internal fields in terms of the statistical error norms: First, for one representative case all measured statistical error norms are presented. Then the results of all experiments are summarized in terms of the rms and maximum norms.

Table 4. Statistical Errors over the Scattering Angles (RMS and Max) for the VIEF Simulations of the Scattering Matrix for the Three Spheres from Table 1[a]

| | $S_{11}$ | | pol = $-S_{12}/S_{11}$ | | $S_{33}/S_{11}$ | | $S_{34}/S_{11}$ | |
|---|---|---|---|---|---|---|---|---|
| Sphere Number | RMS (%) | Max (%) | RMS | Max | RMS | Max | RMS | Max |
| 1 | 12 | 37 | 0.02 | 0.10 | 0.03 | 0.19 | 0.02 | 0.17 |
| 2 | 7.4 | 35 | 0.04 | 0.15 | 0.04 | 0.26 | 0.04 | 0.17 |
| 3 | 6.5 | 15 | 0.05 | 0.12 | 0.05 | 0.17 | 0.11 | 0.22 |

[a]The error norms for $S_{11}$ are computed from the relative error at each scattering angle. For the other matrix elements the errors are absolute.

The cpwl was increased to a value at which the model contains approximately $10^5$ cubes. This is the maximum number that we could handle, in terms of available computer memory and computer time. For the $x = 3$ particle the maximum cpwl was 60, for $x = 5$ it was 35, and for $x = 9$ it was 20. The minimum cpwl was 10 in all cases.

As a representative case we first consider a sphere with $x = 5$ and $m = 1.33 + 0.01i$. In Fig. 7 the absolute and relative errors in the internal field obtained by the VIEF are shown as functions of cpwl. The same behavior of the errors as functions of cpwl was observed in all the other experiments that we performed in this study. The maximum error is more-or-less constant and certainly does not decrease with increasing cpwl. These maximum errors in the internal field are always located on the surface of the sphere. All other statistical error norms (minimum, mean, standard deviation, and rms) show a monotonic decrease with increasing cpwl.

The behavior of the errors in the cross sections and in the scattering matrix is somewhat different in the sense that here the maximum error also decreases as the discretization of the sphere is made finer. As an

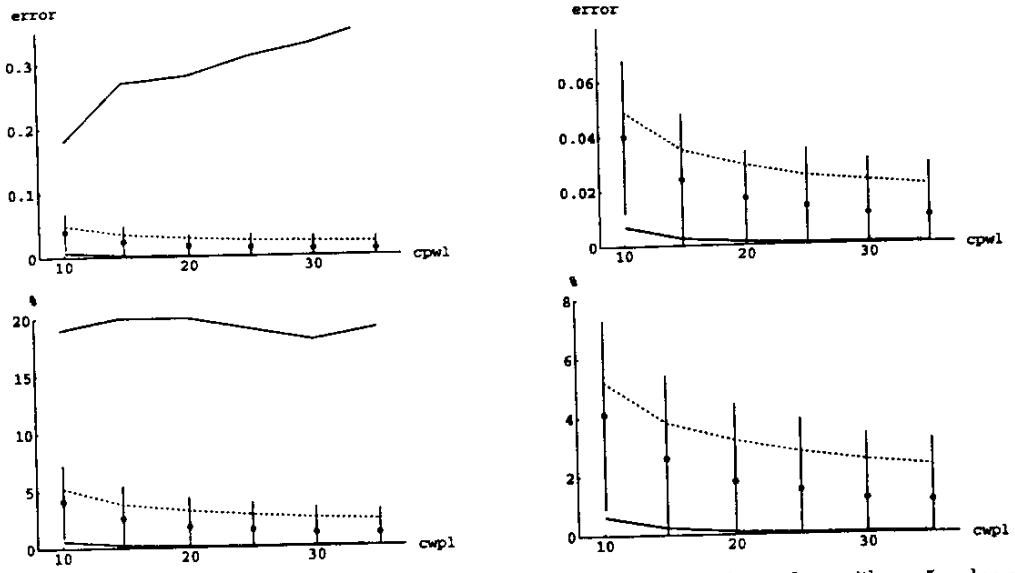


7. Top, absolute and bottom, relative errors in VIEF simulations of the internal field for a sphere with $x = 5$ and $m = 1.33 + 0.01i$ a function of cpwl. Upper solid curves, maximum error; lower solid curves, minimum error. Filled circles, mean errors; bars, standard viations. Dashed curves, the rms. Left, all the data; right, enlargements of data at left.

ample we show, in Fig. 8, the relative errors in $S_{11}$ nd the cross sections. As was already discussed in Subsection 4.B, it is sufficient to know the rms and he maximum error to gain good insight into the average errors. Figures 7 and 8 show this even better. rom now on we therefore report only rms and maximum errors.

As was already discussed in Subsection 2.B, the ubes in the VIEF simulation should be small relative o the wavelength inside the particle. This wavelength equals the wavelength of the incident light in vacuum divided by the real part of the refractive index of the particle. In all our simulations we calculated the size of the cubes by dividing the wavele[illegible]h of the incident light by the cpwl. Therefore if we want to compare VIEF calculations for spheres with different refractive indices we have to divide the cpwl by the real part of the refractive index. In what follows we report on errors in VIEF calculations as a function of this scaled cpwl, and in this way we compare the errors for different size parameters and refractive indices.

Figure 9 shows the errors in VIEF simulations as a function of cpwl/Re($m$) for the internal fields. The accuracy of the internal field shows a clear dependency on the refractive index of the sphere. Keeping in mind that the standard deviation of the error distribution is large, of the order of the rms itself, we can also conclude from Fig. 9 that the relative errors in the internal field depend only weakly on the size parameter (in the range covered by our experiments).

The relative error in $C_{ext}$, $C_{sca}$, and $C_{abs}$ depends strongly on all parameters that we tested (data not shown). However, for the two smaller refractive indices the errors are always smaller than 1%. Only for the largest refractive index do larger errors occur. In that case, even if cpwl/Re($m$) $\geq$ 15, the errors in the cross sections lie between 2% and 5%. In that case, however, the error shows a monotonic decrease with increasing cpwl.

The rms errors in the scattering matrix elements are much less sensitive to both the refractive index and the size of the sphere. The two curves seem to overlap. Therefore in Fig. 10 we have plotted for

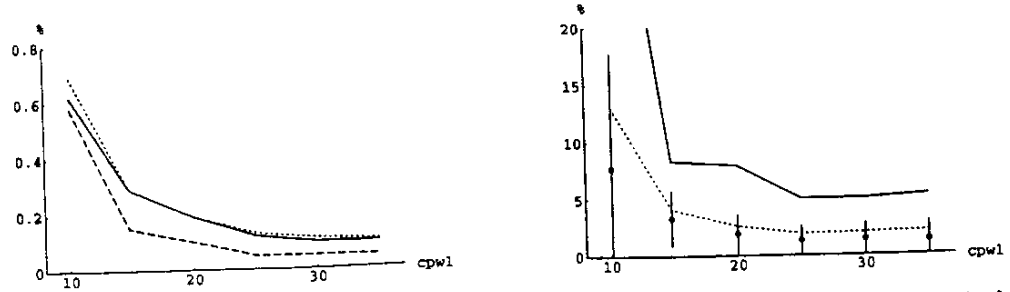


Fig. 8. Relative errors left, in the cross sections (solid curve, $C_{ext}$; dotted curve, $C_{sca}$; dashed curve, $C_{abs}$) and right, in the $S_{11}$ element of the scattering matrix (meaning of the curves as in Fig. 7) as a function of cpwl for a sphere with $x = 5$ and $m = 1.33 + 0.01i$.

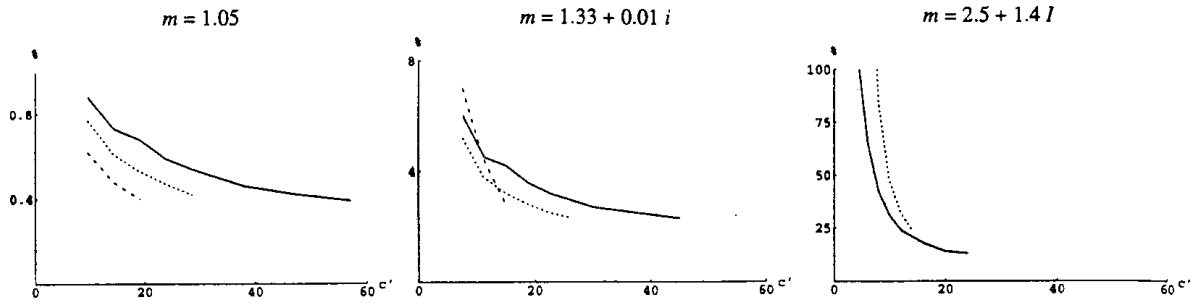


Fig. 9. rms for the relative errors in the internal field as a function of $c'$ = cpwl/Re($m$) for $x = 3$ (solid curves), $x = 5$ (dotted curves), and $x = 9$ (dashed curves).

each scattering matrix element the rms as a function of cpwl/Re($m$) for all the spheres that we studied. We plotted all values as single points, without making a distinction between the size parameter and the refractive index of the sphere. Figure 10 shows that the errors in the scattering matrix elements decrease as cpwl/Re($m$) increases. Furthermore, within the range of size parameters and refractive indices that we studied, the errors for a constant value of cpwl/Re($m$) are very close together, a fact that shows up in Fig. 10 as relatively narrow bands of points.

### D. Size Dependence

The experiments discussed in Subsection 4.C suggest that the dependence of the errors on the size parameter is weak. We performed a set of experiments to test this assumption further. The value of cpwl/Re($m$) was fixed to 15, and VIEF calculations were carried out for spheres with size parameters in the range $1 \leq x \leq 10$. The refractive indices were again taken as above. Note that in these experiments increasing the size parameter means that the numbers of cubes in the VIEF simulation also increases.

The accuracy of the internal field simulation depends weakly on the size parameter. As an example, the results for relative errors in the internal field for $m = 1.33 + 0.01i$ are shown in Fig. 11. From $x = 1$ to $x = 4$ the errors decrease, but for $x \geq 4$ they seem to oscillate about a constant value. For the other two refractive indices the results are comparable. A closer look at the distributions of the errors within the spheres also shows that they are in all cases highly similar to those presented in Fig. 3 (data not shown). The maximum relative error in the internal field has, in all three cases, the same order of magnitude for the full range of $x$ values.

The behavior of the errors in the scattering matrix elements is comparable. In all cases a relevant $x$ dependence cannot be observed. However, in some isolated cases a rms value can suddenly increase for a certain $x$ value. This happens, for instance, for $S_{11}$ for $x = 9$ and $m = 1.33 + 0.01i$. Considering $S_{11}$ as a function of the scattering angle shows that the VIEF simulation has a relatively large error in the backscattering directions (data not shown) that is not present for $x = 8$ and $x = 10$. We have not been able

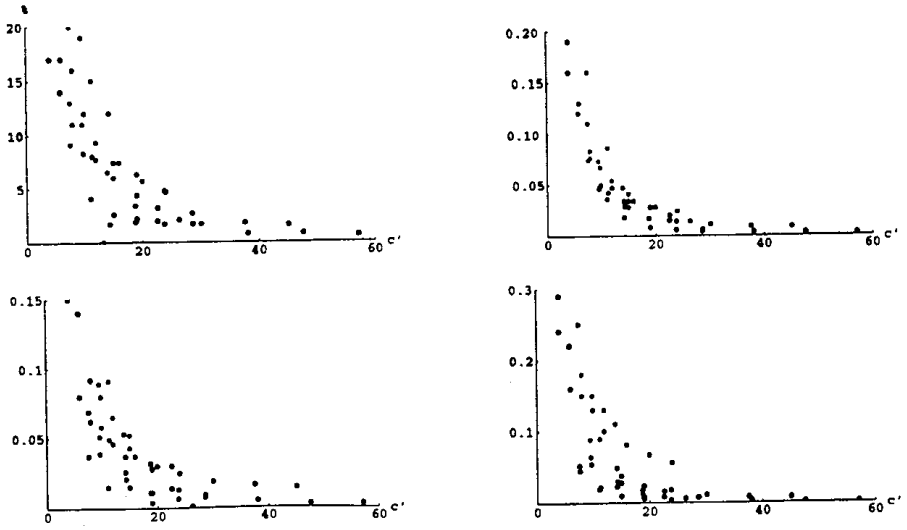


Fig. 10. rms for the scattering matrix elements as a function of $c'$ = cpwl/Re($m$). Upper left, relative errors of $S_{11}$. Absolute errors are shown for polarization (upper right, $S_{33}/S_{11}$ (lower left), and $S_{34}/S_{11}$ (lower right). These plots do not distinguish among the parameters in the simulation (i.e., size and refractive index of the sphere).

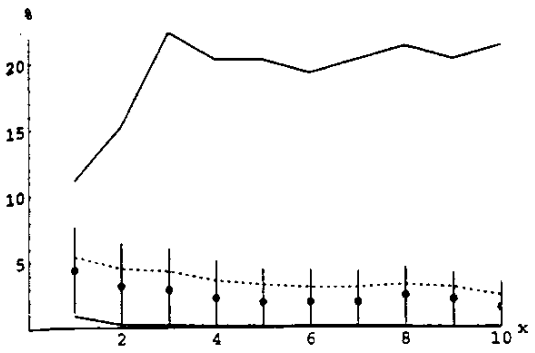


Fig. 11. Relative errors in the internal fields as a function of the size parameter. The refractive index was $m = 1.33 + 0.01i$, and cpwl/Re($m$) = 15. Upper solid curve, maximum error; lower solid curve, minimum error. Filled circles, mean errors; bars, the standard deviation. Dashed curve, the rms.

to find a correlation between this behavior of $S_{11}$ and the errors in the internal fields.

Finally, the errors in the cross sections do show an $x$ dependence. However, within the range of size parameters that we have covered the relative errors in the cross sections have a tendency to decrease with increasing size parameter (data not shown). Assuming that we can exclude the size parameter as an important parameter in the accuracy of VIEF simulations, we can tabulate the errors that we have measured in this set of experiments as a function of the refractive index only (see Table 5). This exercise reveals once more the dependence on the refractive index that was suggested above.

### E. Resonances

Finally we investigate whether VIEF simulations are able to reproduce resonances in Mie scattering (see Subsection 2.C). We identified two resonances that fall within the range of ($x$, $m$) values that can be covered by our VIEF simulations. For a size parameter of $x = 4.875$ we found two values of $m$, close together, for which the Mie scattering becomes resonant, $m = 2.3009279$ and $m = 2.3534695$. Figure 12 shows $C_{ext}$ in the range $2.2 \leq m \leq 2.4$ for Mie calculations and for a number of VIEF simulations. In all VIEF simulations we take cpwl = 36, which corresponds to cpwl/$m$ = 15 for $m = 2.4$.

The Mie calculations show the predicted resonances as two peaks on a smooth background. The VIEF simulations also show two sharp peaks, which are shifted to slightly larger values of $m$. This suggests that the VIEF is able to reproduce the Mie

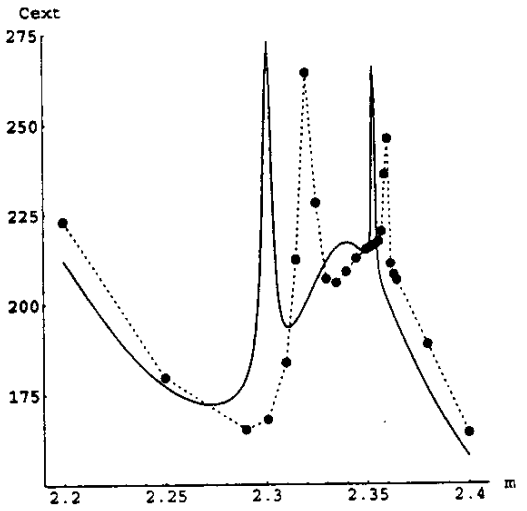


Fig. 12. Extinction coefficient as a function of refractive index for Mie calculations (solid curve) and VIEF simulations (filled circles).

resonances but not at the exact positions. We now examine the internal fields for a number of cases to investigate whether the VIEF simulations indeed reproduce the $a_7$ and $b_8$ Mie resonances. First we examine a case in which both the Mie and VIEF simulations are nonresonant ($m = 2.2$), and then we examine the internal fields for all $m$ values at which either the Mie or the VIEF simulation has a peak in the extinction coefficient.

Figure 13 shows the energy density in a plane through a sphere with $m = 2.2$ (i.e., nonresonant for both Mie and VIEF calculations). The internal field in this case is comparable with the internal fields for $m = 1.33 + 0.01i$ above. However, now the interference peak is shifted more to the center of the sphere, a result that is due to the larger refractive index, which results in a sharper focusing of the electric field in the sphere (see also Ref. 37). Again the largest errors in the VIEF simulations occur on the surface of the sphere; however, we can now also observe stronger errors inside the sphere. The rms of the relative errors in the internal field is 15%. For $S_{11}$ it is 8.8%, for polarization it is 0.14, for $S_{33}$ it is 0.08, and for $S_{34}$ it is 0.07. Finally, the relative error in $C_{ext}$ is 5.2%. These numbers are consistent with those presented in Table 5 (only the rms of the polarization is greater than normal), and this case is no exception.

Next, consider the case $m = 2.3009279$, which corresponds to the first $C_{ext}$ peak for Mie in Fig. 12. Figure 14 shows the energy densities for the Mie

Table 5. Typical Mean RMS Errors in the Range $1 \leq x \leq 10$

| $m$ | RMS Internal Field (%) | RMS $S_{11}$ (%) | $RMS_{pol}$ | RMS $S_{33}$ | RMS $S_{34}$ | Cross Section (%) |
|---|---|---|---|---|---|---|
| 1.05 | 0.6 | 10 | 0.03 | 0.02 | 0.03 | <0.3 |
| 1.33 + 0.01$i$ | 4 | 5 | 0.05 | 0.04 | 0.04 | <1 |
| 2.5 + 1.4$i$ | 22 | 7 | 0.03 | 0.04 | 0.06 | <8 |

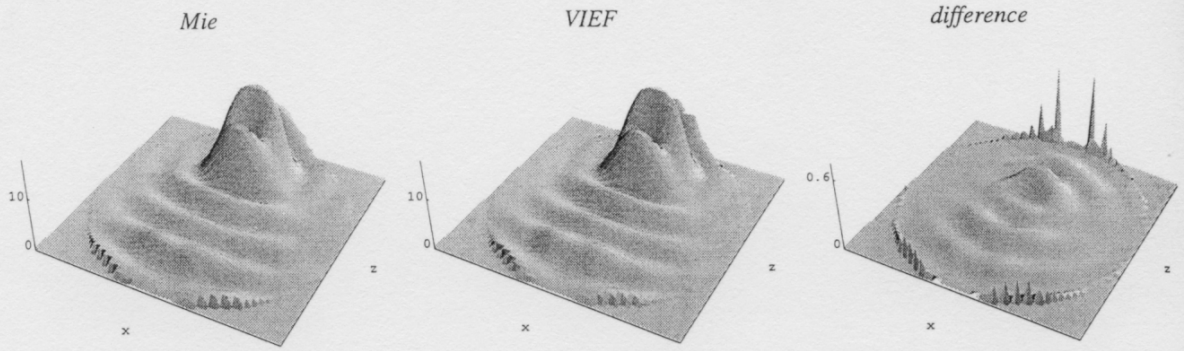


Fig. 13. Energy density for the internal field obtained by Mie calculation, VIEF simulation, and the difference field for $m = 2.2$. The energy density is plotted in the $y = 0.08727$ plane. The data are not normalized; all scales in the plots are linear.

calculations and VIEF simulations. First notice the large differences in scale between them. The $a_7$ resonance in the Mie calculation can be recognized from the seven peaks in the energy density in each half of the sphere. The maximum energy density for the Mie calculation is approximately 250. The VIEF results are now completely different. The energy density looks similar to that in the $m = 2.2$ case (see Fig. 13), although we can observe a split of the interference peak in the back of the sphere and a second peak appearing in the front of the sphere, which can be interpreted as the onset of a resonance. The resultant scattering matrix from the VIEF simulation is now completely wrong (data not shown).

Figure 15 shows the energy density for the second Mie resonance, i.e., $m = 2.3534695$. Again, notice the large difference in scales for the Mie resonance and the (nonresonant) VIEF simulation. Furthermore, notice that now we have plotted the energy density in a $y$–$z$ plane (i.e., an $x$ = constant plane) because the resonances of the $b$ type are perpendicular to the incident linear polarization. The $b_8$ resonance is now recognized by the fact that most energy density is located in the $x$ = constant plane and in eight peaks in each half of the sphere.

Finally, the refractive indices for which the VIEF $C_{ext}$ curve shows its maxima are analyzed. First consider the case $m = 2.32$, which corresponds to the first $C_{ext}$ peak for the VIEF in Fig. 12. Figure 16 shows the energy densities for the Mie calculations and the VIEF simulations. The $a_7$ resonance is now clearly observed in the VIEF results, with an amplitude that is comparable with the true Mie resonance from Fig. 14. The Mie results are typically nonresonant and resemble those for $m = 2.2$ (see Fig. 13).

Figure 17 shows the energy density for the second VIEF resonance, i.e., $m = 2.36$. In this case the $b_8$ resonance is clearly recognizable in the VIEF results, although the amplitudes are much smaller than those of the corresponding Mie resonance in Fig. 15. We did not carry out any more VIEF simulations in the immediate vicinity of $m = 2.36$. It is possible that for a slightly different refractive index the VIEF resonance will be as strong as the Mie resonance.

## 5. Discussion and Conclusions

The results of the extended sets of experiments to test the accuracy of VIEF simulations of the internal field can be summarized as follows: The accuracy of the internal field simulations decreases with increasing refractive index. The largest errors always occur on the surface of the sphere, and the maximum errors seem to be independent of the size of the cubic cells. However, the average errors (mean, rms) in the internal field decrease if the cubic cells decrease in size. For a fixed value of cubes per wavelength the errors

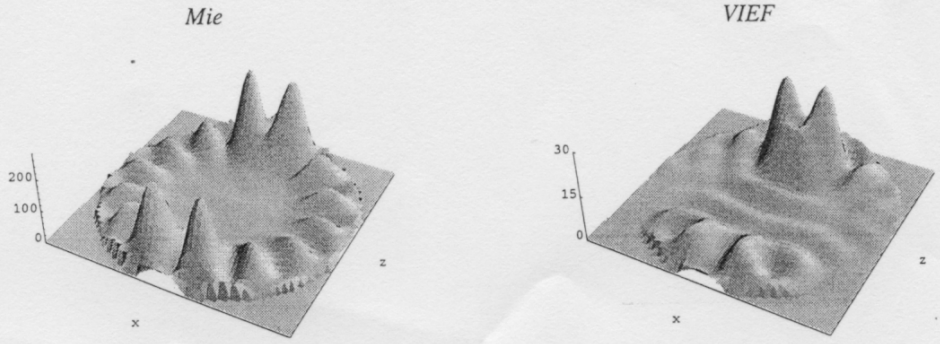


Fig. 14. Energy density for the internal field obtained by Mie calculation and VIEF simulation for $m = 2.3009279$. The energy density is plotted in the $y = 0.08727$ plane. The data are not normalized; all scales in the plots are linear.

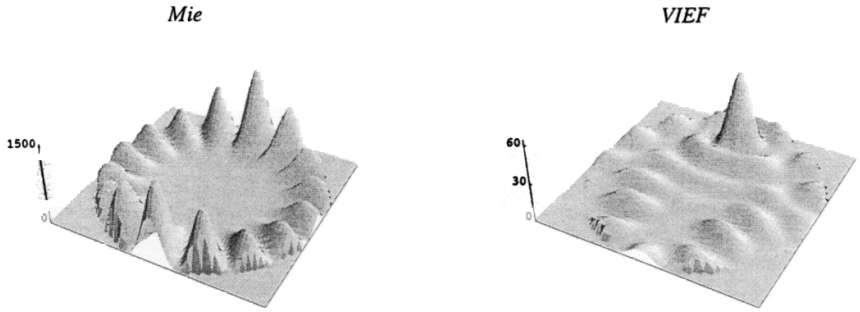


Fig. 15. Same as Fig. 14 but for $m = 2.3534695$. The energy density is now plotted in the $x = 0.08727$ plane.

in the internal field depend only weakly on the size of the sphere.

Our results are in agreement with those of Draine (see Subsection 2.B and Ref. 30). Draine, however, attributes the errors, especially on the surface, to the surface granularity of the model of the sphere. However, our results show that even for fine discretizations the maximum errors, located at the surface of the sphere, stay large. This result suggests that surface granularity does not provide a full explanation for the error behavior. We believe that the assumption of piecewise-constant electric fields in the cubic cells to discretize Eq. (1) (something that is implicitly done in the DDA) also contributes to the large errors in the surface layers of the model. More-accurate basis functions, such as those used by Peltoniemi,[20] might result in better accuracy of the fields in the surface layers.

Furthermore, the singularity of the Green's function can also cause large errors on the surface. The Green's function has an $r^{-3}$ radial dependency near the singularity. Our VIEF scheme generates some errors owing to the use of piecewise-constant basis functions and crude one-point numerical integration formulas. Inside the sphere these errors can cancel because of symmetry. However, on the surface this cancellation does not occur, and the errors become visible, a result that may also explain why the maximum errors stay large if the discretization is made finer. Although the smaller cubes can represent the

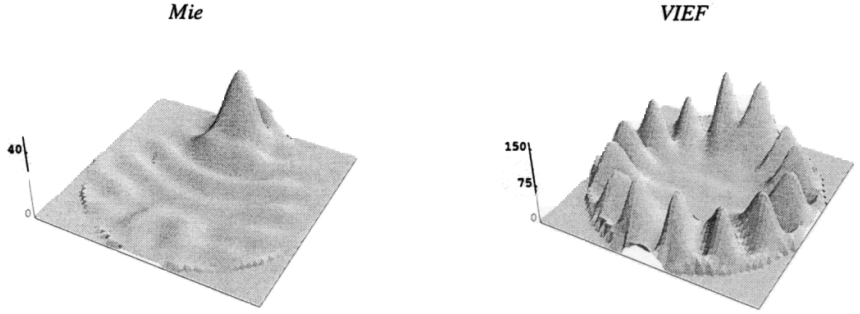


Fig. 16. Same as Fig. 14 but for $m = 2.32$.

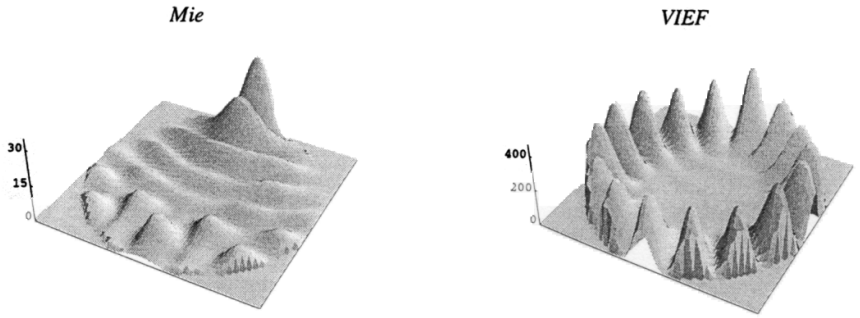


Fig. 17. Same as Fig. 14 but for $m = 2.36$. The energy density is now plotted in the $x = 0.08727$ plane.

rapidly changing electric field more accurately, the singularity of the Green's function becomes more pronounced because of the reduced distance between neighboring cells.

The discretization of the sphere should be fine enough to represent the waves inside the sphere, which have a wavelength $\lambda/\mathrm{Re}(m)$. The size of the cubes is represented by $d = \lambda/\mathrm{cpwl}$. Therefore, to compare the accuracy for different refractive indices, we present the results as a function of $\mathrm{cpwl}/\mathrm{Re}(m)$. Figure 9 shows that, even on this scale, the accuracy of the internal fields still depends strongly on the refractive index.

In Ref. 30 Draine provides arguments to support the reasoning that, if the imaginary part of the refractive index becomes high, another length scale inside the particle, the skin depth, will determine the size of the cubic cells. Therefore he proposes to take $\lambda/|m|$ as the typical length scale inside the particle and to keep the cubic cells small with respect to it. Even if this procedure is taken into account, e.g. in Fig. 9, we continue to see a strong dependency of the relative rms errors in the internal field on the refractive index of the sphere. Another effect than discretization of the sphere plays a role in determining the accuracy of the internal fields.

Within the range of our simulations, the size parameter has a much less pronounced influence then the other model parameters on the accuracy of the internal fields. Therefore we assume that we can rule out the size parameter. [See Table 5, where the accuracy of the VIEF is given as a function of the refractive index for $\mathrm{cpwl}/\mathrm{Re}(m) = 15$.] It would be interesting to explore this assumption further and determine whether it holds for other values of $\mathrm{cpwl}/\mathrm{Re}(m)$, for larger ranges of the size parameter, and for other particle shapes. If such were the case, the expected accuracy of VIEF (or DDA) simulations could be taken from accuracy tables such as Table 5.

The VIEF simulations are capable of reproducing strong realistic resonances in the internal fields, as was shown in Subsection 4.E. However, the positions of the resonances on the refractive-index axes (see Fig. 12) were slightly too large (0.9% and 0.4% for the first and the second peaks, respectively). As was pointed out by an anonymous reviewer, one can obtain such a shift in resonance peaks by slightly reducing the size parameter in the Mie calculation. Therefore a small error in the size parameter that is used in the Mie calculation could account for the effect. However, because the cpwl was large in these VIEF simulations, the discretization of the sphere was fine and the error in the resultant equal volume size parameter was therefore too small to account for the shift in the resonance peaks.

The width and the height of the peaks in $C_{\mathrm{ext}}$ as functions of $m$ for VIEF simulations are equal to those for the Mie calculation. We did, however, observe that the number of iterations needed for convergence of the VIEF simulations increased sharply near the resonance positions. The analysis in Ref. 19 suggests that at resonance the VIEF coefficient matrix becomes singular, which explains the increase in the number of iterations.

Our results on the accuracy of the cross sections and scattering matrix elements are in good agreement with those of other authors. However, our method of analyzing the data shows some features that are not immediately obvious from previously published results. The accuracy of the cross sections and the scattering matrix elements decreases with decreasing size of the cubic cells. Also, the maximum error in the scattering matrix elements decreases. As with the internal fields, the accuracy depends only weakly on the size parameter of the sphere. Furthermore, the absolute errors in scattering matrix elements polarization, $S_{33}/S_{11}$, and $S_{34}/S_{11}$ are much less sensitive to the refractive index than to the internal fields (see, e.g., Fig. 10 and Table 5). On the other hand, the accuracy of the cross sections does show a dependency on the refractive index that correlates with the accuracy in the internal fields. The dependency of the accuracy of the $S_{11}$ element is less clear.

Finally, we analyze how the accuracy of the internal fields translates to that of the cross sections and the scattered fields. One would expect that, if the errors in the internal fields decreased, likewise the errors in the scattered fields would decrease. This relationship is observed if the accuracy is measured as a function of the size of the cubic cells. However, if the accuracy is measured as a function of the refractive index the correlation is much less clear and perhaps not even present. A possible explanation can be found in errors in the phase relations and direction of the internal fields. Our definition of the errors in the internal fields is based on the amplitude of the difference between the Mie and the VIEF internal fields. This means that information with respect to the phase and the direction of the internal field is discarded. As the scattered fields are a result of interference between fields radiated from each cubic cell, it might well be that the statistical errors in the internal field need to be supplemented with information on the errors in the phase and direction of the internal field if we are to understand fully the accuracy of the cross sections and the scattering matrix.

The accuracy of VIEF simulations could be increased by use of other types of basis functions and numerical formulations. In many cases the geometries could be represented more accurately with tetrahedral elements instead of the cubic ones. The electric field could be represented with piecewise-linear or higher-order basis functions, which would allow one to use larger computational cells. Also, the use of more-accurate numerical integration formulas and Galerkin or least-squares formulations instead of the collocation technique would improve the accuracy of the VIEF method.

### References and Notes

1. L. Shafai, ed., thematic issues on computational electromagnetics, Comput. Phys. Commun. **68**(1–3) (1991).

2. J. W. Hovenier, **ed., special issue on light scattering by nonspherical particles, J. Quant. Spectrosc. Radiat. Transfer 55(5)** (1996).
3. K. Lumme, **J. W. Hovenier, K. Muinonen, J. Rahola, and H.** Laitinen, eds., *Proceedings of the Workshop on Light Scattering by Non-Spherical Particles* **(University of Helsinki, Helsinki,** 1997).
4. P. C. Waterman, **"Symmetry, unitarity, and geometry in electromagnetic scattering,"** Phys. Rev. D **3,** 825–839 (1971).
5. M. I. Mishchenko, **"Light scattering by randomly oriented axially symmetric particles," J. Opt. Soc. Am. A 8, 871–882** (1991).
6. C. Hafner, ***The Generalized Multipole Technique for Computational Electromagnetics*** (Artech, Norwood, Mass., **1990).**
7. A. Doicu and T. Wriedt, **"Formulation of the extended boundary condition method for incident Gaussian beams using** multiple-multipole **expansions," J. Mod. Opt. 44, 785–801** (1997).
8. B. T. Draine and P. **J. Flatau, "Discrete-dipole approximation** for scattering calculations," J. Opt. Soc. Am. A 11, **1491–1499** (1994).
9. A. Lakhtakia and G. **W. Mulholland, "On two numerical techniques** for light scattering by dielectric **agglomerated structures,"** J. Res. **Natl. Inst. Stand. Technol. 98, 699–716 (1993).**
10. D. **E. Livesay and K. Chen, "Electromagnetic field induced** inside arbitrarily shaped biological bodies," IEEE Trans. Microwave Theory **Tech. MTT-22, 1273–1280 (1974).**
11. G. H. **Goedecke and S. G. O'Brien, "Scattering by irregular** inhomogeneous particles via the digitized Green's function algorithm," Appl. Opt. **27,** 2431–2438 (1988).
12. J. I. Hage and J. M. Greenberg, **"A model for the optical properties** of porous grains," Astrophys. J. **361,** 251–259 (1990).
13. J. I. Hage, **"The optics of porous particles and the nature of** comets," Ph.D. dissertation (University of Leiden, Leiden, **The** Netherlands, 1991).
14. P. **W. Dusel, M. Kerker, and D. D. Cooke, "Distribution of** absorption centers within irradiated spheres," **J. Opt. Soc. Am. 69,** 55–59 (1979).
15. J. D. Pendleton, **"Water droplets irradiated by a pulsed $CO_2$** laser: **comparison of computed temperature contours with explosive** vaporization patterns," Appl. Opt. **24,** 1631–1637 (1985).
16. R. Thurn and W. Kiefer, **"Structural resonances observed in** the Raman spectra of optically levitated liquid droplets," Appl. Opt. **24,** 1515–1519 (1985).
17. J. B. **Snow, S. X. Qian, and R. K. Chang, "Stimulated Raman** scattering from **individual water and ethanol droplets," Opt.** Lett. **10,** 37–39 (1985).
18. H. M. Tzeng, K. **F. Wall, M. B. Long, and R. K. Chang, "Laser** emission **from individual water and ethanol droplets at** morphology-dependent **resonances," Opt. Lett. 9, 499–510** (1984).
19. J. Rahola, **"Efficient solution of dense systems of linear equations** in electromagnetic scattering calculations," **Ph.D. dissertation (Helsinki University of Technology, Espoo, Finland,** 1996).
20. J. I. Peltoniemi, **"Variational volume integral equation method** for electromagnetic scattering by irregular grains," **J. Quant.** Spectrosc **Radiat. Transfer 55, 637–647 (1996).**
21. E. M. Purcell and C. R. Pennypacker, **"Scattering and absorption of light by nonspherical dielectric grains," Astrophys. J. 186,** 705–714 (1973).
22. K. Lumme and J. Rahola, **"Light scattering by porous dust particles in the discrete-dipole approximation," Astrophys. J. 425, 653–667 (1994).**
23. **A. Lakhtakia, "Macroscopic theory of the coupled dipole approximation method," Opt. Commun. 79,** 1–5 (1990).
24. **A. Lakhtakia, "Strong and weak forms of the method of moments and the coupled dipole method for scattering of time-harmonic electromagnetic fields," Int. J. Mod. Phys. C 3, 583–603 (1992).**
25. **J. Rahola, "Solution of dense systems of linear equations in the discrete dipole approximation," SIAM J. Sci. Stat. Comput. 17,** 79–89 (1996).
26. **R. W. Freund, "Conjugate gradient type methods for linear systems with complex symmetric coefficient matrices," SIAM J. Sci. Stat. Comput. 13,** 425–488 (1992).
27. **J. J. Goodman, B. T. Drain, and P. J. Flatau, "Application of fast-Fourier-transform techniques to the discrete-dipole approximation," Opt. Lett. 16,** 1198–1200 (1991).
28. **A. G. Hoekstra, M. D. Grimminck, and P. M. A. Sloot, "Simulating light scattering from micron-sized particles: a parallel fast discrete dipole approximation," in *Proceedings of High Performance Computing and Networking Europe 1996*, H. Lidell, A. Colbrook, B. Hertzberger, and P. Sloot, eds., Vol. 1067 of Lecture Notes in Computer Science (Springer-Verlag, Berlin, 1996), pp. 269–275.**
29. **A. G. Hoekstra, M. D. Grimminck, and P. M. A. Sloot, "Large scale simulations of elastic light scattering by a fast discrete dipole approximations," Int. J. Mod. Phys. C 9,** 87–102 (1998).
30. **B. T. Draine, "The discrete dipole approximation and its application to interstellar graphite grains," Astrophys. J. 333, 848–872 (1988).**
31. **B. T. Draine and J. Goodman, "Beyond Clausius-Mossotti: wave propagation on a polarizable point lattice and the discrete dipole approximation," Astrophys. J. 405,** 685–697 (1993).
32. **A. G. Hoekstra and P. M. A. Sloot, "Dipolar unit size in coupled dipole calculations of the scattering matrix elements," Opt. Lett. 18,** 1211–1213 (1993).
33. **C. F. Bohren and D. R. Huffman, *Absorption and Scattering of Light by Small Particles* (Wiley, New York, 1983).**
34. **B. A. Hunter, M. A. Box, and B. Maier, "Resonance structure in weakly absorbing spheres," J. Opt. Soc. Am. A 5,** 1281–1286 (1988).
35. **P. R. Conwell, P. W. Barber, and C. K. Rushforth, "Resonant spectra of dielectric spheres," J. Opt. Soc. Am. A 1,** 62–67 (1984).
36. **G. Videen, J. Li, and P. Chylek, "Resonances and poles of weakly absorbing spheres," J. Opt. Soc. Am. A 12,** 916–921 (1995).
37. **C. C. Dobson and J. W. I. Lewis, "Survey of the Mie problem source function," J. Opt. Soc. Am. A 6,** 463–466 (1989).
38. **C. Liu, T. Kaiser, S. Lange, and G. Schweiger, "Structural resonances in a dielectric sphere illuminated by an evanescent wave," Opt. Commun. 117,** 521–531 (1995).
39. **WWW pages containing other figures and additional internal field visualizations: http://www.wins.uva.nl/~alfons/int/int-f.html.**